Design Optimization of a Surface-Mounted Permanent-Magnet Motor With Concentrated Windings for Electric Vehicle Applications

Jiabin Wang, *Senior Member, IEEE*, Xibo Yuan, *Member, IEEE*, and Kais Atallah

Abstract—This paper describes design techniques for electric vehicle (EV) traction machines to achieve high efficiency against a defined driving cycle such as the New European Drive Cycle (NEDC) while satisfying the required torque–speed operating range. A fractional-slot concentrated-winding (FSCW) surface-mounted permanent-magnet (SPM) machine has been identified as a suitable candidate for EV applications due to its high power/torque density, high efficiency, and good flux-weakening capability compared with other competing machine topologies. Based on the vehicle characteristics and the reference driving cycle, the motor specifications are established, and the design constraints for the SPM machine to satisfy the peak torque and flux-weakening capabilities are derived. Furthermore, the influence of the key parameters, such as slot–pole number combination, machine inductance, axial length, and number of turns, on the machine copper and iron losses over the NEDC is evaluated. Optimizations were carried for these parameters to minimize the total energy losses over the driving cycle. It has been shown that conventional design methodologies that aim to maximize efficiency in the region close to the rated operating condition may lead to less optimal designs and higher energy losses over the NEDC. A prototype motor for a front- and rear-wheel-driven EV has been designed, manufactured, and tested. The experimental results validate the proposed design methodology.

Index Terms—Design optimization, driving cycle, electric vehicles (EVs), permanent-magnet (PM) motor.

I. Introduction

WITH increasing concerns on energy security and environmental impacts, internal combustion engine (ICE)-based vehicles that consume fuel derived from natural resources will have a limited role in future transportation. Electric vehicles (EVs) [1], on the other hand, have the potential to offer an ultimate solution for sustainable personal mobility in the future, particularly if they can be powered by electrical energy generated from renewable sources, such as solar, wind, wave, and tidal streams, with no need for extra fossil-fuel-based power plants.

The provision of power-dense highly efficient electric traction machines is essential for the development and swift realization of EVs. Of the competing electrical machine technologies for traction applications [2]–[4], induction machines are potentially of the lowest cost, and they are able to operate over a wide speed range. However, they have a lower torque density and an inferior power factor and efficiency compared with permanent-magnet (PM) brushless machines. Similarly, while switched reluctance machines are more robust than PM brushless machines, they have a higher torque ripple and a poorer power factor, which increases the inverter cost. Thus, in general, PM brushless machines are preferred for traction applications, where energy efficiency and power density are the most important attributes [5]–[10].

The challenge for the EV traction machine design is that it has to produce high torque, i.e., usually $3 \sim 4$ times the nominal value, at a standstill or low speed to provide the required acceleration and climbing capability [11]. Conversely, the machine needs to output peak power close to twice the rated value at medium to high speed. The wide torque and speed operating range places significant constraints on achievable machine efficiency and power density using conventional design methodologies.

Since an EV operates over a wide torque–speed range in response to various driving conditions, the machine design should be aimed to achieve overall energy saving over a driving cycle. The high-efficiency operating region of current state-of-the-art PM brushless machines for EV traction is typically designed around the rated operating point [9] or a few points around the rated point [13]. However, EV traction machines during typical urban or suburb driving frequently operate in the low torque region, where the efficiency is much lower. This is due to the fact that when the vehicle is not accelerating, the required torque for overcoming rolling resistance and air drag is much lower than the peak torque during climbing while accelerating. Clearly, the mismatch between the regions of high efficiency and high operating duty with the existing PM brushless traction drives results in low overall efficiency, high energy consumption, and reduced vehicle range. Therefore, it is important to develop a viable motor design method, allowing for minimizing the total energy loss over a driving cycle rather than at a few operating points.

This paper describes design techniques for EV traction machines to achieve high efficiency against a defined driving

J. Wang and K. Atallah are with the Department of Electronic and Electrical Engineering, The University of Sheffield, Sheffield S1 3JD, U.K. (e-mail: j.b.wang@sheffield.ac.uk).

X. Yuan was with the Department of Electronic and Electrical Engineering, The University of Sheffield, Sheffield S1 3JD, U.K. He is now with the Department of Electrical and Electronic Engineering, University of Bristol, Bristol BS8 1UB, U.K.
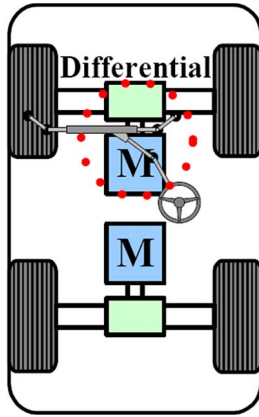
Fig. 1. Schematic of a front and rear drive train.

cycle, such as the New European Drive Cycle (NEDC), while satisfying the required torque–speed operating range.

Section II describes the procedure to derive the motor torque, speed, and power ratings from the defined cycle and layout the main specifications. Section III identifies constraints that should be considered for surface-mounted PM (SPM) motor design to meet the peak torque and flux-weakening capabilities. Section IV analyzes the influence of the leading parameters on the machine performance. The slot–pole number combinations, machine inductance, axial length, and number of turns are carefully compared and selected to minimize the total energy loss over the NEDC. A fractional-slot concentrated-winding (FSCW) SPM with the proposed design methodology has been manufactured. The experimental test results are presented in Section V, which validate the predicted motor performance.

II. MOTOR DESIGN SPECIFICATIONS

Without loss of generality, the traction machines for a microsized vehicle with front and rear drives are considered. The vehicle employs two traction motors that are connected to the front and rear axles via a differential, as shown in Fig. 1. Thus, the front and rear wheels are independently driven. In the event of a front- or rear-drive system failure, the vehicle can continue to operate using the remaining healthy drive system with no sudden stops or compromising vehicle stability and safety. Furthermore, this power-train architecture facilitates various functions that are required to enhance the driving performance. First, the steering ability can be enhanced by appropriate selection of two- and four-wheel drives according to road surface conditions. Second, drivability can be improved by distribution of driving torque to the front and rear wheels according to operating conditions. In addition, stability is also secured by precisely distributing the braking torque to the front and rear wheels upon detection of a wheel slip or a wheel lock. The distributed front and rear wheel drives will also maximize energy recovery during braking and improve power-train efficiency by dynamic apportioning the traction torques against various driving conditions. The two traction machines are under torque control, and their speed ratings are automatically synchronized against vehicle speed and tire interaction with the road surface.

From the vehicle data and performance requirements, the peak and continuous torque–speed envelopes for one motor
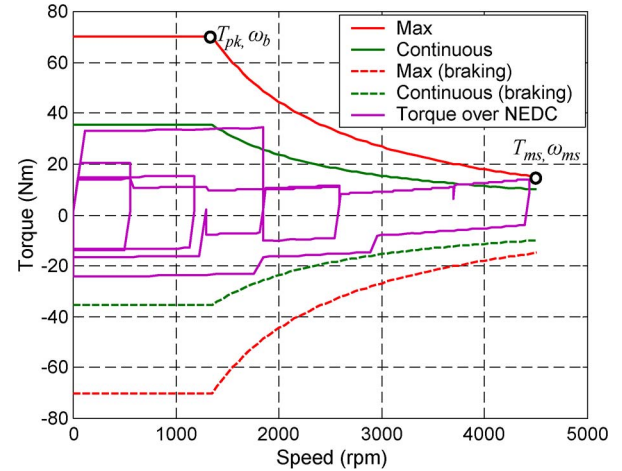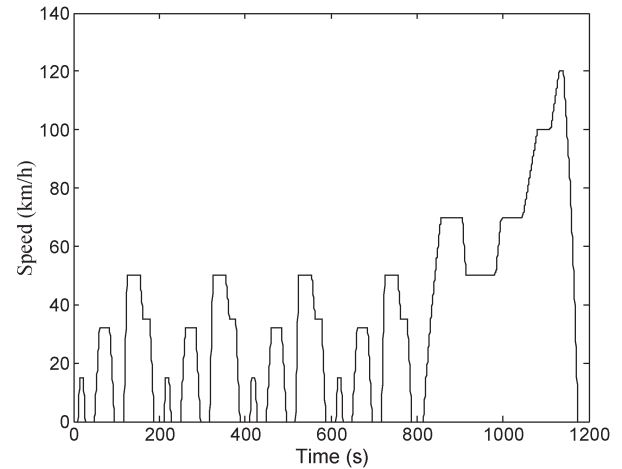

Fig. 2. Torque speed envelope.

Fig. 3. NEDC.

TABLE I
DESIGN SPECIFICATIONS

Base speed:	ω_b	1350 rpm
Maximum cruise speed:	ω_{ms}	4500 rpm
Maximum speed	ω_{max}	5050 rpm
Peak torque below and at base speed:	T_{pk}	70Nm
Continuous torque below and at base speed:	T_c	35.5Nm
Peak power	P_{pk}	9.9kW
Continuous power:	P_c	5kW
Peak torque at maximum cruise speed:	T_{ms}	15 Nm
Continuous power at maximum cruise speed	P_{cms}	4.7kW
Nominal DC link voltage	V_{dc}	120V,
Maximum permissible line-to-line voltage	E_{max}	< 250V (for safety)

with 50% torque split between the front and rear axles are established, as shown in Fig. 2, using the procedure described in [14]. The NEDC, as shown in Fig. 3, is employed as a reference cycle against which the design optimization should be performed.

Thus, for the purpose of comparison, the torque speed trajectory over the NEDC is also shown in Fig. 2. It is shown that most part of this trajectory is under the continuous torque–speed envelope, which implies that the vehicle can run the NEDC continuously without reaching the thermal limit. More specific targets can be obtained in Fig. 2, and they are summarized in Table I.

It should be noted that the peak torque–speed envelope is effectively defined by two points: the peak torque at the base speed (ω_b, T_{pk}) and the peak torque at the maximum cruise speed (ω_{ms}, T_{ms}), as indicated in Fig. 2. The power-train configuration allows intelligent torque distribution between the front and rear motor drives for efficiency improvement [15].

III. SURFACE-MOUNTED PERMANENT-MAGNET MOTOR DESIGN CONSTRAINTS

There are numerous PM machine topologies that differ in PM rotor structures and stator winding arrangements [5]. An SPM synchronous motor with fractional slot (per pole) concentrated winding (FSCW) is merging as a promising candidate suitable for EV applications, due to its good flux-weakening and over-load capability [16], [17]. Compared with the interior-mounted PM (IPM) motor with distributed winding, the FSCW SPM benefits from shorter end winding, less cogging torque, and higher torque density and efficiency [18], [19]. Furthermore, in an FSCW machine, the coils belonging to each phase are concentrated and wound on consecutive teeth, or alternate teeth, so that the phase windings do not overlap. This is not only a distinctive manufacturing advantage but is also conducive to a high copper packing factor, and hence high efficiency, and to reducing the likelihood of an interphase fault. Recent studies on the IPM with concentrated windings have shown that saliency, which is essential for the reluctance torque, is significantly reduced due to the ratio of pole number to slot number being close to 1 [20], [21]. This machine topology also suffers from a high iron loss in the rotor core due to high-order space harmonics from the concentrated winding configuration.

To design an SPM machine satisfying the specifications listed in Table I, the design constraints related to the lead-ing design parameters must be identified to meet various performance requirements, such as the flux-weakening and peak torque capabilities. Since the traction machine is re-quired to provide constant-power operation over a wide speed range, a very important issue in this particular application is their field-weakening capability. Good field weakening re-quires the machine inductance to satisfy the following condition [17], [22]:

$$L_d \geq \frac{\psi_m}{I_{rated}} \qquad (1)$$

where L_d is the d-axis inductance, Ψ_m is the flux linkage due to PMs, and I_{rated} is the rated machine current.

For an SPM machine, the induced back electromotive force (EMF) E at the maximum speed ω_{max} is given by

$$E = p\psi_m\omega_{max}. \qquad (2)$$

Since the permanent magnetic field cannot be turned off in the event of a fault, this voltage must be limited below the maximum permissible peak line-to-line voltage E_{max}. Thus

$$E = p\psi_m\omega_{max} \leq \frac{E_{max}}{\sqrt{3}} \quad \text{or} \quad p\psi_m \leq \frac{E_{max}}{\sqrt{3}\omega_{max}} \qquad (3)$$

where p is the number of pole pairs. Meanwhile, the electro-magnetic torque of the surface-mounted machine is given by

$$T_{em} = \frac{3}{2}p\psi_m I_m. \qquad (4)$$

It is shown in (3) and (4) that there is a conflict demand on the product of the number of pole pairs and the flux linkage, i.e., $p\psi_m$: a small value is preferred for low induced back EMF at maximum speed, whereas a large value is desirable for high torque and high efficiency.

To meet the peak torque capability T_{pk}, the maximum peak motor current I_{max} must be satisfied, i.e.,

$$T_{em} = \frac{3}{2}p\psi_m I_{max} \geq T_{pk} \quad \text{or} \quad I_{max} \geq \frac{2}{3}\frac{T_{pk}}{p\psi_m}. \qquad (5)$$

Substituting (3) into (5) yields

$$I_{max} \geq \frac{2}{\sqrt{3}}\frac{T_{pk}\omega_{max}}{E_{max}}. \qquad (6)$$

Assuming space-vector modulation, the maximum achiev-able peak phase voltage V_{max} in the linear region is $V_{max} = V_{dc}/\sqrt{3}$. The required inverter voltampere (VA) rating can therefore be derived from

$$\frac{3}{2}V_m I_m \geq \frac{3}{2}\frac{V_{dc}}{\sqrt{3}}\frac{2}{\sqrt{3}}\frac{T_{pk}\omega_{max}}{E_{max}} = \frac{V_{dc}}{E_{max}}T_{pk}\omega_{max}. \qquad (7)$$

Furthermore, to achieve the peak torque T_{ms} at the maximum cruise speed of ω_{ms} under the current limit of I_{max}, the required d- and q-axis currents are given by

$$i_{qms} = \frac{2}{3}T_{ms}/p\psi_m \quad i_{dm} = -\sqrt{I_{max}^2 - i_{qms}^2}. \qquad (8)$$

The minimum d-axis inductance $L_{d\,min}$ can be found by con-sidering the voltage constraint of

$$L_{d\,min}^2\left(I_{max}^2 - i_{dm}^2\right) + \left[(\psi_m - L_{d\,min}i_{dm})^2\right] \leq \left(\frac{V_m}{p\omega_{ms}}\right) \qquad (9)$$

and is given by

$$L_{d\,min} = \frac{-\psi_m i_{dm} - \sqrt{(\psi_m i_{dm})^2 - I_{max}^2\left[\psi_m^2 - (V_m/p\omega_{ms})^2\right]}}{I_{max}^2}. \qquad (10)$$

The machine synchronous inductance must be greater than this value, i.e., $L_d > L_{d\,min}$. In addition, at the base speed ω_b, the following voltage constraint has to be satisfied:

$$(p\omega_b I_{max}L_d)^2 + (p\omega_b\psi_m + I_{max}R)^2 \leq V_m^2. \qquad (11)$$

This imposes a maximum limit on the d-axis inductance, i.e.,

$$L_{d\,max} = \frac{\sqrt{(V_m)^2 - \left[I_{max}R + (E_{max}\omega_b/\omega_{max}/\sqrt{3})\right]^2}}{p\omega_b I_{max}}. \qquad (12)$$

Thus, (10) and (12) define the inductance range that can meet the required peak torque and flux-weakening capabilities.
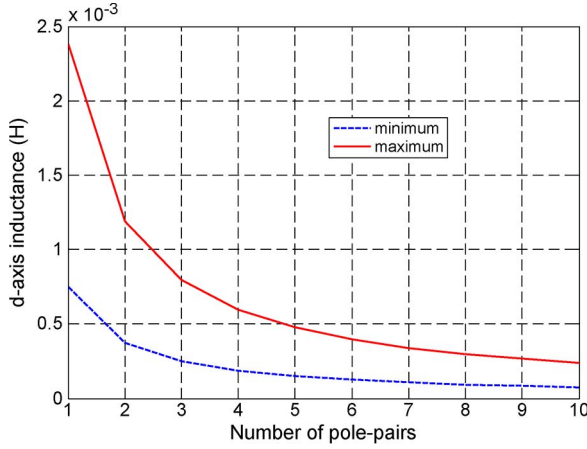
Fig. 4. Variation of the minimum and maximum inductances with the number of pole pairs for SPM machine topology.

Fig. 4 shows the maximum and minimum d-axis inductances as a function of the number of pole pairs for the design specifications given in Table I.

It follows that for a given pole pair p, the maximum flux linkage per pole, the minimum phase current, and the minimum inverter VA rating, as well as the maximum and minimum d-axis inductances of an SPM machine, are all directly constrained by the design specifications.

IV. DESIGN OPTIMIZATION OF A SURFACE-MOUNTED PERMANENT-MAGNET MOTOR AGAINST THE NEW EUROPEAN DRIVE CYCLE

The theoretical background of FSCW SPM machines and their feasible slot–pole combinations have been well established in [16], [17], and [19]. In particular, the analytical framework that was reported in [16], [17], [19], and [23] allowed computationally efficient prediction of machine performance and, hence, derivation of an optimal design against the specification. In this paper, the special consideration with regard to the motor design is given on the minimization of motor energy losses over the NEDC while satisfying the required constraints.

A. Influence of Leading Design Parameters

The design of a three-phase FSCW SPM can be optimized with respect to the leading design parameters shown in Fig. 5, taking account of both core saturation and subject to a specified thermal constraint, R_e being the outer radius of the stator and G being the air-gap length. It should be noted that the required tooth width T_w and radial thickness H_y of the stator yoke are dependent on the air-gap flux density and maximum permissible flux density in the teeth and yoke.

For a given stator outer radius R_e, the design parameters that have the most significant influence on the performance are the dimensional ratios R_m/R_e and α_m/β_p (where β_p is the pole pitch), the magnet thickness H_m, the air-gap length G, and the number of pole pairs. In general, the performance improves as H_m is increased. However, an increase in the volume of the PM material will increase the cost, particularly if it is a rare-earth magnet, and result in a heavier rotor, which is usually
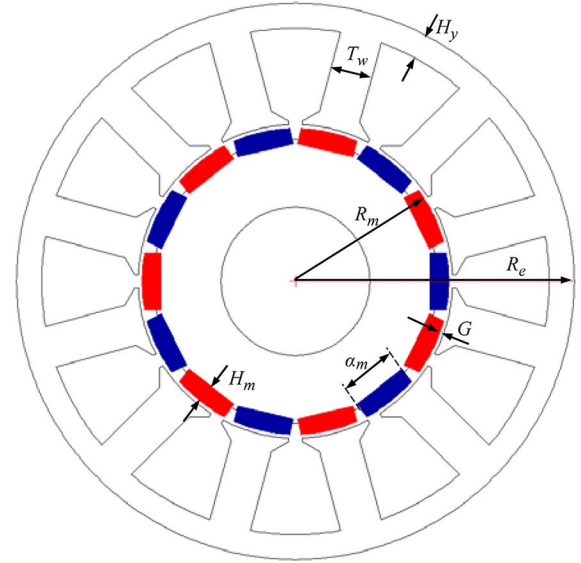

Fig. 5. Leading design parameters.

undesirable for rapid acceleration. In this paper, therefore, the magnet thickness is fixed at 6 mm to produce acceptable air-gap flux density and torque density while providing the required demagnetization withstand capability. The air-gap length G is also assumed to be constant, at 1.0 mm, since although a smaller air gap would also improve the performance, ultimately, it is limited by manufacturing tolerances, the thickness of the banding layer, as well as stiffness and static and dynamic radial run-out considerations.

The magnet pole-arc to pole-pitch ratio α_m/β_p should be optimized to minimize torque ripple, which results from the cogging torque and the EMF harmonics [24]–[26]. This optimal ratio is virtually independent of other design parameters and is set to 0.833 for all designs considered in this paper. The design optimization process scans three leading parameters, viz., R_m/R_e, T_w, and H_y, for minimum energy loss over the NEDC, as defined in (13) subject to the specifications defined in Table I and the thermal constraint and a fixed set of design parameters given in Table II. Thus

$$\min(P_{\text{loss}}) \text{ subject to defined constraints}$$

$$P_{\text{loss}} = \int_{\text{NEDC}} (p_{\text{cu}} + p_{\text{fe}})\, dt \tag{13}$$

where p_{cu} and p_{fe} are the copper and iron losses of the motor, respectively. The iron loss is calculated using the technique reported in [27]. It should be noted that the influence of the active length l_e on the machine performance is independent of the other design parameters, and it will be separately considered in Section IV-D.

B. Slot–Pole Number Combinations

It has been shown in [16] and [23] that both 12-slot/10-pole and 12-slot/14-pole design variants represent very good slot–pole number combinations for the application under consideration. The two designs have the same number of slots

TABLE II
FIXED DESIGN PARAMETERS AND CONSTRAINTS

Air-gap length	G	0.001 m
Outer diameter	R_e	0.150 m
Stack length	l_e	0.135 m
Magnet thickness	H_m	0.006 m
Magnet pole arc	α_m	150 electric degree
Ambient temperature	T_{am}	45 ^{0}C
Temperature rise at 35.5 Nm	T_r	< 105 ^{0}C
Cooling condition		Air-cooled

in the stator and, hence, very similar winding resistance and inductance characteristics. For the 14-pole machine, however, the flux per pole to produce the same torque at the same current will be lower due to the high pole number, and hence, its ψ_m/L_d ratio is lower, which is conducive to better flux-weakening capability. Furthermore, compared with the 10-pole machine, the flux density level in the 14-pole machine will also be lower, but its fundamental frequency at a given speed will be higher. The resultant iron loss in the 14-pole machine may be less or similar to that of the 10-pole counterpart.

It is important to note that since the EV operates over a wide torque speed range, a design optimized against the rated torque at the base speed does not necessarily lead to an optimal design over a given driving cycle. Likewise, a design optimized against a driving cycle does not yield the best performance when a different drive cycle or condition takes place. Thus, similar to the design of conventional ICE vehicles, the design and performance are very much dependent on drive styles. As mentioned in this paper, the design is optimized with respect to minimum energy consumption over the NEDC since this driving cycle is often used for evaluating the fuel economy of a vehicle. The three leading design parameters for both 10- and 14-pole machines are optimized for minimum energy loss over the NEDC.

Fig. 6 compares the torque–speed envelopes of the two designs (14 and 10 poles) at the maximum and minimum dc-link voltages. The active length and outer diameter of both designs are kept at 136 mm and 150 mm, respectively, and the leading design parameters are given in Table III. For both designs, the optimal split ratio R_m/R_e is the same, whereas the flux per pole of the 10-pole design is proportionally higher than that of the 14-pole counterpart. However, the tooth width T_w and back-iron thickness H_y of the 14-pole design do not proportionally decrease compared with those of the 10-pole design. This is due to the fact that the frequency of the 14-pole design is increased, and to reduce iron loss at high speed, the flux density in the stator core has to be lower. The resultant number of turns that satisfy all constraints for both the designs is the same albeit it has to be quantized into an integer. Consequently, the synchronous inductance of the two designs is essentially the same. As shown, the 14-pole design has a slightly high torque capability, whereas its maximum torque at high speed is slightly lower. This is mainly due to the quantization effect (i.e., the number of turns has to be an integer) of the selection of the number of turns to fit the required torque speed envelope, as shown in Fig. 6. As shown, both designs satisfy the required torque capability over the speed range in general, except for the 14-pole design, which exhibits slightly lower peak torque
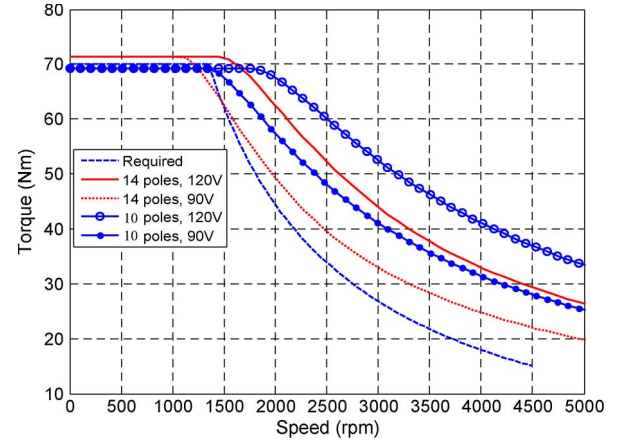

Fig. 6. Torque–speed envelopes of 12-slot/10-pole and 12-slot/14-pole designs.

TABLE III
LEADING DESIGN PARAMETERS OF 12-SLOT/10-POLE AND
12-SLOT/14-POLE VARIANTS

	12-slot, 10-pole	12-slot, 14-pole
R_m/R_e	0.55	0.55
T_w (mm)	11.8	11.2
H_y (mm)	7.0	6.75
Number of turns	7	7

at the base speed when the dc-link voltage is at the minimum of 90 V. It should be noted that when the battery voltage is low, the required field-weakening effect, and, hence, the d-axis current, will be great for the same output torque [28], [29]. Consequently, the copper loss is increased, and the motor efficiency is decreased.

Fig. 7 compares the d- and q-axis currents, the iron and copper losses, the magnitude of current, and the power factor of the two designs over the NEDC. The negative power factor indicates the regenerative operation during braking. As will be seen, the q-axis currents of the two designs for producing the required traction torque over the NEDC are very similar. However, as mentioned, the 14-pole design yields a lower d-axis current over the flux-weakening region, which leads to a low current magnitude and, hence, a lower copper loss at high speed.

It is also shown that the iron loss of the 14-pole design is also slightly lower due to lower flux density in the stator tooth and back iron. Thus, the total energy consumption of the 14-pole machine over the NEDC is 57.67 kJ, as opposed to 66.47 kJ of the 10-pole design. Clearly, the 14-pole design is a better choice, with a 13.3% reduction in energy consumption.

C. Influence of the Machine Inductance

It has been shown in Fig. 4 that there are minimum and maximum limits on the machine inductance against a required set of specifications. For high power factor and low inverter VA rating, a lower inductance would be preferred. In contrast, a large inductance would provide a better field-weakening capability and, hence, a reduction in copper loss at high speed. Table IV compares the minimum, maximum, and predicted machine inductances of the two design variants. As shown,
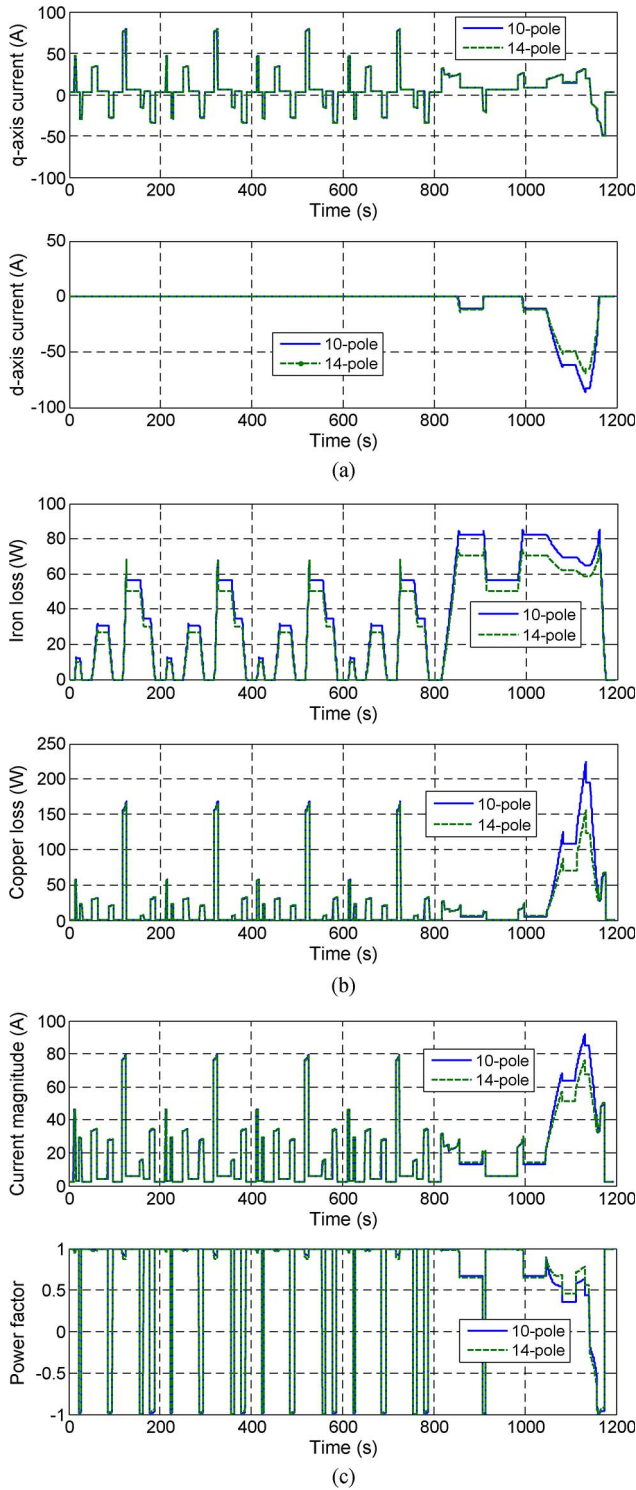
Fig. 7. Comparison of two design candidates (10 and 14 poles). (a) *q*-axis and *d*-axis currents. (b) Iron and copper losses. (c) Magnitude of current and power factor.

TABLE IV
COMPARISON OF MACHINE INDUCTANCE AND RESISTANCE OF
TWO DESIGN VARIANTS

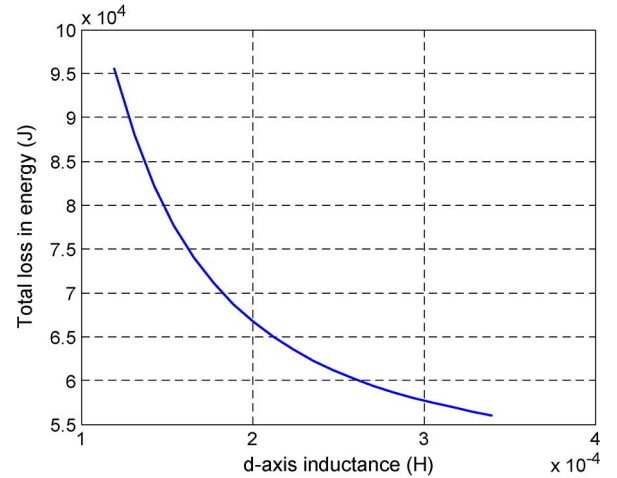|	12-slots/14-poles	12-slots/10-poles
Min. inductance (mH)	0.107	0.150
Max. Inductance (mH)	0.340	0.476
Predicted inductance (mH)	0.301	0.301
Winding resistance at 120^{0}C (mΩ)	17.8	17.8

Fig. 8. Variation of the total energy consumption over the NEDC with the *d*-axis inductance of the 14-pole machine.

should therefore be designed to its maximum limit. It should be noted that the power factor of the SPM machine is very high, and the variation of inductance within the minimum and maximum limits shown in Fig. 4 has an insignificant influence on the converter losses.

D. Optimal Tuning of Axial Length and Number of Turns

There are several ways to increase the machine inductance, for example, by 1) reducing the air-gap length or the magnet thickness, or 2) reducing the slot opening width or increasing the tooth-tip height. The first method increases the air-gap permeance shown by the stator winding and, as such, would also affect the other machine performance. Furthermore, since the magnets exhibit permeability close to air, the variation of machine inductance is not very sensitive to the air-gap length or the magnet thickness. While the second method is effective in increasing the inductance, it also leads to greater leakage flux and a high level of magnetic saturation in the tooth-tip region and, hence, an undesirable increase in iron loss.

To increase the machine inductance without adversely affecting other performance, the number of turns may be increased. However, this will also increase the flux linkage per pole and hence reduce the peak torque capability at the base speed. To circumvent the problem, the axial length may be proportionally reduced since the winding flux due to permanent magnets is proportional to the product of the axial length and the number of turns, whereas the machine inductance is proportional to the product of the axial length and the square of the number of turns. For example, in the previous design for the 14-pole

the predicted machine inductance of 0.301 mH of the 14-pole design is closer to its maximum limit of 0.34 mH.

Fig. 8 shows the variation of the total energy consumption of the 14-pole machine over the NEDC with the machine inductance within the minimum and maximum limits. It is evident that the energy consumption decreases as the machine inductance increases. The optimal value of the inductance

TABLE V
COMPARISON OF MACHINE PARAMETERS OF TWO 14-POLE DESIGN
VARIANTS WITH DIFFERENT NUMBERS OF TURNS

Design variants	Design 1	Design 2
Number of turns	7	8
Active axial length of stator (mm)	135	118
Predicted inductance (mH)	0.301	0.344
Winding resistance at 120^{0}C (mΩ)	17.8	20.8
Flux linkage per phase (mWb)	39.6	39.6
Current at maximum torque of 70Nm (A, peak)	170	170

machine, the number of turns per coil per phase is 7, and the axial length is 135 mm. By increasing the number of turns to 8 and at the same time reducing the axial length from 135 to 118 mm, the net flux linkage is unchanged, whereas the inductance is increased by a factor of 8/7. Table V compares the key machine parameters of the two designs.

As shown, the two designs have the same phase flux-linkage and torque production capabilities. However, design 2 has a higher inductance approximately equal to the maximum inductance limit and, hence, better flux-weakening capability. Since the number of turns is increased in design 2, the phase resistance also increases, which will lead to a greater copper loss. However, the iron loss will decrease as the flux density is not changed, whereas the axial length is reduced.

Fig. 9 compares the d- and q-axis currents and the iron and copper losses of the two design variants over the NEDC. As will be shown, the q-axis currents of the two designs for producing the required traction torque over the NEDC are essentially the same. However, design 2 yields a lower d-axis current over the field (flux)-weakening region, which leads to a low current magnitude and, hence, a lower copper loss at high speed. On the other hand, its copper loss is higher than that of design 1 at low speed, whereas the iron loss of design 2 is consistently lower than that of design 1.

Table VI compares the total iron loss, copper loss, energy consumption, energy efficiency over the NEDC, efficiency at the rated torque of 35.5 N · m and the base speed of 1350 r/min, as well as the torque density of the two design variants. It is evident that although design 1 has high efficiency than design 2 at the rated operating point, design 2 yields 5% lower energy consumption and 14% higher torque density with ∼14% lower material cost compared with design 1 as a result of the design optimization process. The aforementioned result implies that if the optimization is aimed at maximum efficiency at the rated operation, design 1 would be chosen.

It should be noted that by increasing the number of turns and proportionally reducing the active length, the synchronous inductance is increased, which leads to about a 10% lower copper loss in field weakening and a reduction in iron loss. The combined effect is that not only the efficiency over the NEDC is improved but also the cost and size of the machine is reduced. As regards the thermal rating, the most thermal demanding condition is driving at high speed with low torque. By reducing the copper and iron losses at high speed, the thermal condition of the machine is also improved since the reduction in the total thermal dissipation area is less than 5%.
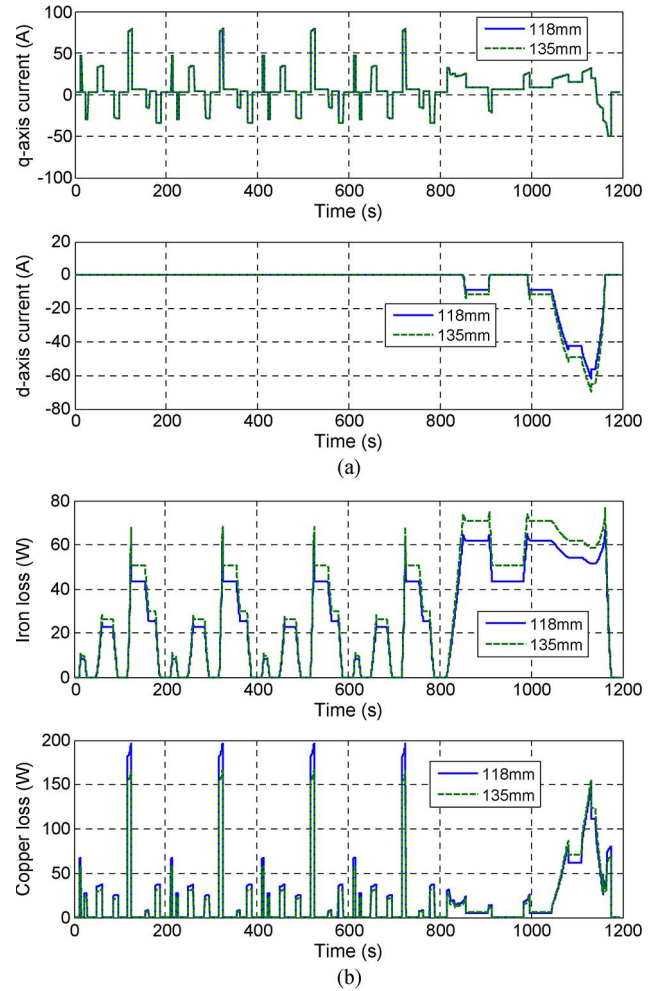

Fig. 9. Comparison of loss and energy consumption of two 14-pole designs. (a) d- and q-axis currents. (b) Iron and copper losses.

TABLE VI
COMPARISON OF LOSSES AND TORQUE DENSITY OF
TWO 14-POLE DESIGNS

	Design 2 (118mm N=8)	Design 1 (135mm N=7)
Iron loss (kJ)	31.12	35.98
Copper loss (kJ)	22.98	21.59
Energy consumption (kJ)	54.25	57.67
Efficiency (%) at 35.5Nm and 1350 rpm	94.4	95.3
Torque density (kNm/m^3)	33.6	29.3

Three observations can be made from the foregoing analysis and discussion.

1) The motor loss at high speed or in field-weakening operation is a significant contributing factor to the total loss over the NEDC.
2) A large d-axis inductance is conducive to a low loss in field-weakening operation.
3) To reduce iron loss at high speed, the flux density level in the cores should be kept relatively low.

To minimize the loss over the NEDC, it is essential that the loss in the low-torque and high-speed regions should be reduced. This illustrates the fact that the design optimization of the EV traction drives is quite different from the conventional

TABLE VII
SUMMARY OF KEY DESIGN AND OPERATIONAL PARAMETERS

| Machine topology:	Surface mounted, fractional slot per pole
Number of pole-pairs	7
Number of slots	12
Axial length (active, mm)	118
Outer diameter (excluding case, mm)	150
Number of turns per coil	8
Number of coils per phase	4
Torque constant (Nm/A peak)	0.415
Efficiency at 1350rpm/35.5Nm (%)	94.4
Continuous current (A peak/rms)	85/60.5
Maximum current (A peak/rms)	170/121
Phase resistance at 120 °C (mΩ)	20.8
Synchronous inductance (mH)	0.344
Flux linkage per phase (mWb)	39.6
Back-emf constant (V peak s/rad)	0.277
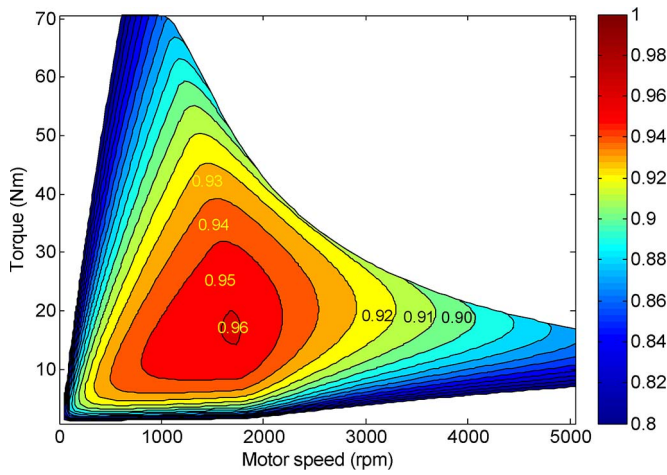
Fig. 10. Predicted efficiency map of the optimized design.

techniques. For example, if one were to minimize the loss at the rated operating point, a reduction in copper loss would be the target. This would push the saturation in the stator and rotor cores to a relatively high level with the effect of lower inductance and high iron loss. Consequently, the loss at high speed and field-weakening operation would increase. Optimizations against different driving cycles, e.g., Artemis Urban, have been also undertaken, and the results have further confirmed the aforementioned finding. However, due to length limits, they will be reported in the near future.

E. Summary of the Final Design

The final optimized design outputs in terms of key dimensional and operational parameters of the 12-slot 14-pole FSCW machine are summarized in Table VII.

The predicated efficiency map of the machine over the required torque speed range is shown in Fig. 10. It can be observed that the efficiency of 95% and above occurs over the torque range of 10–30 N · m and the speed range of 800–2000 r/min. The machine exhibits efficiency greater than or equal to 90% over a wide torque–speed range. Note that the mechanical and windage losses and the eddy current loss in the rotor magnets are not accounted for in the efficiency map prediction. The machine also has very low cogging torque, and
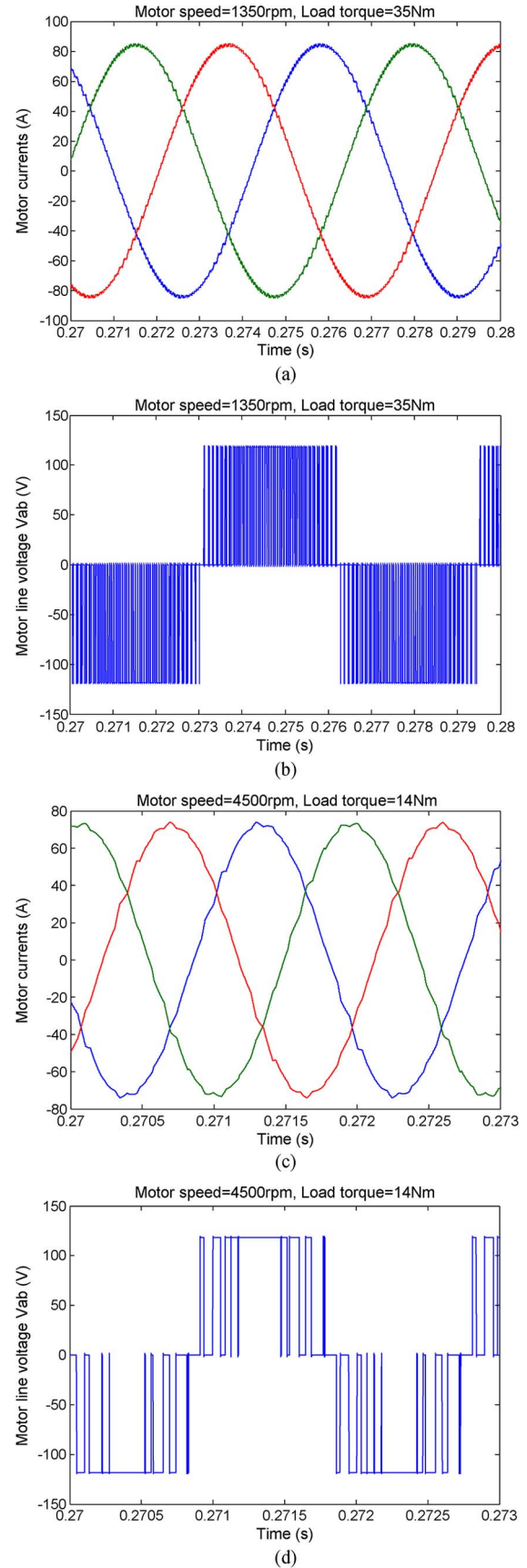

Fig. 11. Simulated current and voltage waveforms under two typical operating conditions. (a) Current waveform at 35 N · m, 1350 r/min. (b) Line-to line voltage waveform at 35 N · m, 1350 r/min. (c) Current waveform at 14 N · m, 4500 r/min. (d) Line-to line voltage waveform at 14 N · m, 4500 r/min.

(a)

(b)

(c)

Fig. 12.　Prototype motor. (a) Motor stator. (b) Rotor. (c) Motor outer view.

the maximum peak-to-peak torque ripple is below 1.5% of the peak torque. The maximum line-to-line voltage limit is satisfied with a 2% tolerance of 250 V.

Fig. 11 shows current and voltage waveforms under two typical operating conditions with the inverter switching frequency of 10 kHz.

V. PERMANENT-MAGNET MOTOR PROTOTYPE AND EXPERIMENTAL VALIDATION

An FSCW SPM motor has been manufactured according to the design described previously. Fig. 12 shows the stator, rotor (before a carbon fiber bonding layer of 0.4 mm was placed), and complete assembly. The resulting mechanical air gap is 0.6 mm. As shown, each coil is wounded over one tooth, and the end winding is much shorter than conventional distributed winding arrangements. Each rotor pole magnet in Fig. 12(b) is segmented into four pieces in circumference and three pieces in axial length to reduce the eddy current losses due to the magnetomotive force harmonics that occurs in FSCW machines [30], [31].

A test rig has been established to measure the motor performance in the defined torque and speed range. The schematic of the motor test system is shown in Fig. 13.
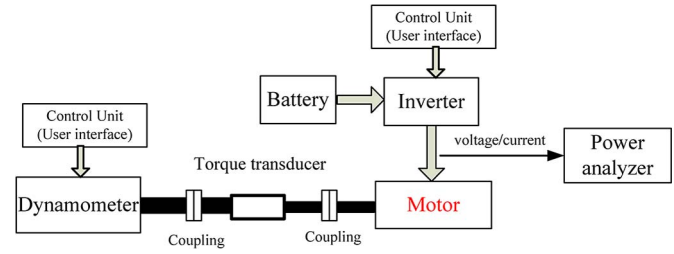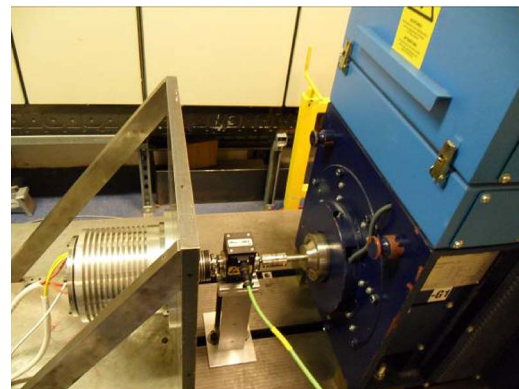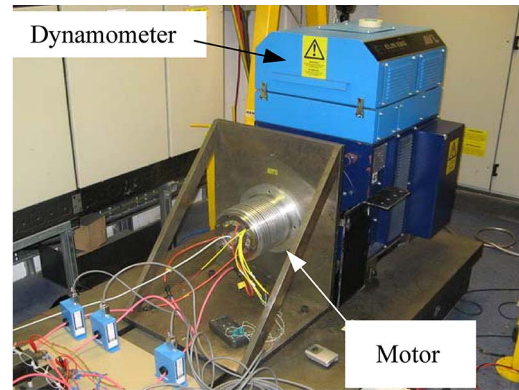

Fig. 13.　Schematic of the motor test rig.

Fig. 14.　Motor test rig.

The dynamometer, which is controlled by a bidirectional four-quadrant converter, is used to drive the motor at a given speed and provides load torque during the load test. The motor is controlled by a commercial inverter that operates in torque control mode and can achieve flux-weakening operation in a high-speed range. The inverter dc-link power is fed by a battery pack. The three-phase input power to the motor (from the inverter) is measured by a power analyzer via the high-precision, high-bandwidth voltage and current transducers. The motor output power is obtained through the inline torque transducer by measuring the torque and speed. The test rig shown in Fig. 14 allows direct measurements of the motor efficiency.

During the no-load test, the motor was driven by the dynamometer over the speed range from 50 to 4500 r/min. The motor phase back-EMF (peak) variation with speed is plotted in Fig. 15(a), whereas the line-to-line back-EMF waveform at 1000 r/min is shown in Fig. 15(b). In Fig. 15, it is shown that motor back EMF has a linear relationship with speed as expected. The back-EMF constant can therefore be determined to be 0.31. This is about 10% higher than the predicted value
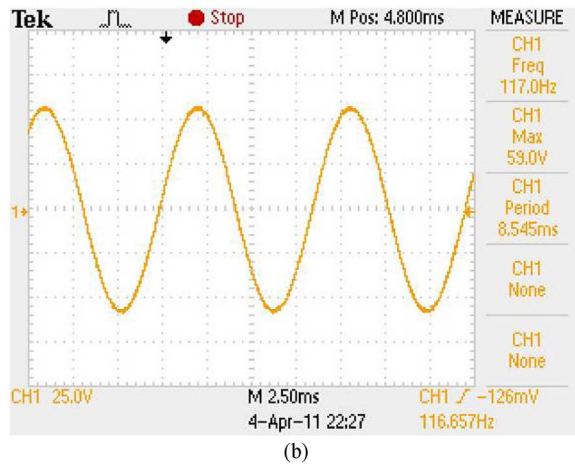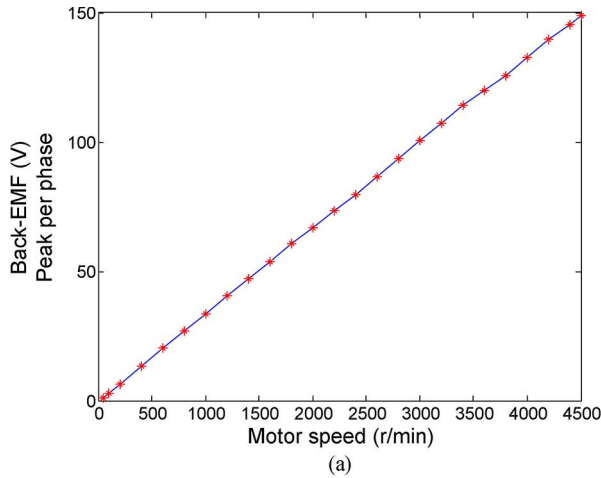
Fig. 15.   Measured motor back EMF during the no-load test. (a) Variation of peak back EMF with speed. (b) Line-to-line back-EMF waveform at 1000 r/min.
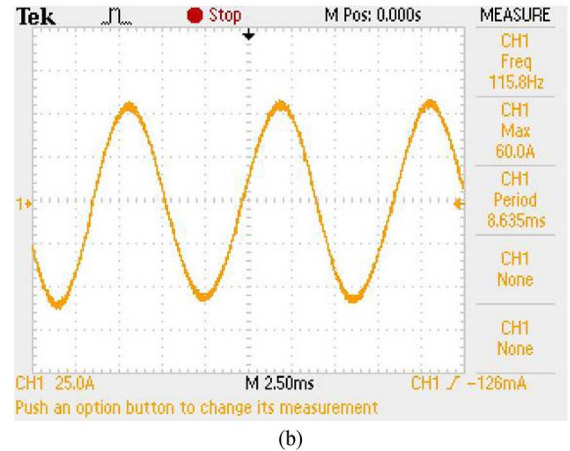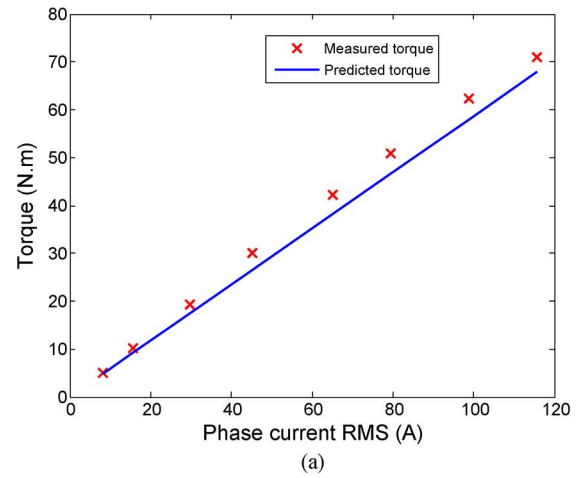

Fig. 16.   Torque and current at speed 1000 r/min. (a) Torque variation with RMS current at 20°. (b) Motor current waveform at 1000 r/min and 24.6 N · m.

of 0.277 at 100 °C, as given in Table VI. However, since the test was carried out at room temperature ~20 °C, the predicted back-EMF constant at this temperature is 0.305, which indicates a very good agreement between measurement and prediction. It is also shown in Fig. 15(b) that the line-to-line back-EMF waveform is essentially sinusoidal with very low harmonic distortion as expected.

The load test was carried out to evaluate motor and drive operation and to measure their efficiency within the torque–speed envelope. The maximum torque (torque capability) that can be achieved at different speed ratings are also measured. First, the relationship between torque and RMS current at speed of 1000 r/min is shown in Fig. 16(a), and the measured phase-A current waveform at 1000 r/min and 24.6 N · m is shown in Fig. 16(b). As shown in Fig. 16, torque has an essentially linear relationship with current, and the torque constant can then be derived as the slope of the line via linear curve fitting, which results in 0.455 N · m/A peak at ~20 °C. Again, this is about 10% higher than the predicted value of 0.415 at 100 °C. However, it favorably compares with the predicted value of 0.451 at 20 °C.

Fig. 17 shows the measured motor efficiency map when the dc-link voltage is 90 V. Compared with the predicted efficiency map in Fig. 10, the measured efficiency map agrees reasonably
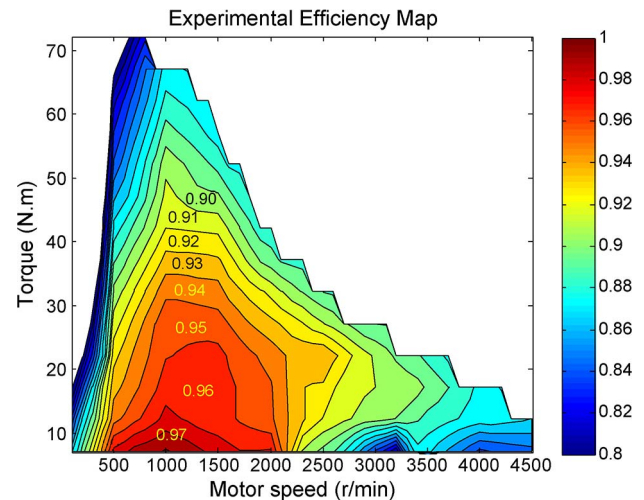

Fig. 17.   Measured efficiency map.

well with the prediction at speed below 2500 r/min. However, at high speed, there are some differences. The main cause of the difference is the fact that the quality of the inverter current control performance deteriorates under flux-weakening operation when the voltage limit is reached. This results in a large d-axis current and, hence, a greater copper loss than what can be achieved theoretically. In addition, the errors of torque

TABLE VIII
COMPARISON OF EFFICIENCY VARIATION WITH TORQUE AT
RATED SPEED OF 1350 r/min

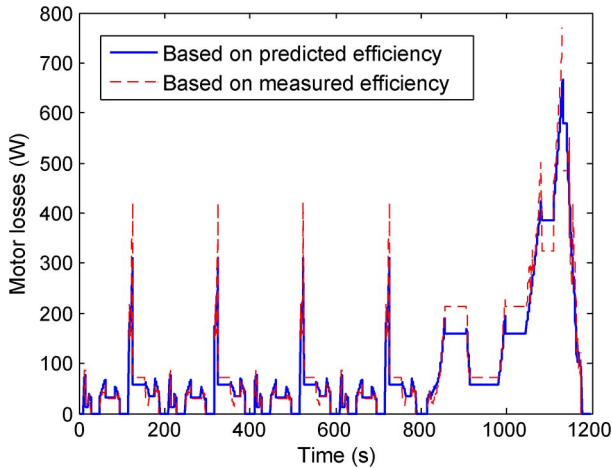| Torque (N.m)	Predicted Efficiency	Measured Efficiency
10	95.5%	97.0%
20	95.6%	96.0%
30	94.8%	95.0%
40	93.6%	92.0%
50	92.0%	90.0%
60	89.3%	88.0%
70	87.0%	85.0%

Fig. 18.   Measured motor losses over the NEDC.

and speed measurement, as well as windage and frictional loss, which are likely more significant at high speed, may also contribute to the difference.

Table VIII compares the measured and predicted efficiency variations with torque at the base speed of 1350 r/min. As shown, the measured motor efficiency agrees well with the prediction. When the torque is below 30 N · m, the measured efficiency is slightly higher than the prediction. An opposite trend is observed when the torque is greater than 30 N · m.

Based on the predicated and measured efficiency map, the motor loss variations over the NEDC are compared in Fig. 18. The two agree reasonably well. The differences exist mainly in the flux-weakening region, where the inverter current control performance degraded and increased the measured losses. The four repeated peak loss points correspond to the peak torque of 34.4 N · m at the speed of 1846 r/min, which represents the maximum acceleration in the NEDC. The motor operates in its light field-weakening region, and the measured efficiency is about 2% lower than the prediction. Consequently, the measured motor loss is 120 W higher. A large difference in the motor energy losses occurs in high speed, where the measured efficiency is lower than the prediction. The total energy consumption calculated over the NEDC based on the measured efficiency map is 72.7 kJ. Compared with the predicated total copper and iron losses of 59.45 kJ at the dc-link voltage of 90 V, 72.7 kJ also includes the windage, friction loss, and rotor magnet losses. As mentioned, the increase in copper loss in the flux-weakening region due to the current tracking error during the experiment also contributes to the difference.

VI. CONCLUSION

This paper has presented a methodology for the design optimization of EV traction motors against a defined driving cycle. An FSCW SPM machine, with high power and torque density, has been designed and manufactured according to the proposed design methodology. It has been shown that the machine inductance must be within a certain range to meet both the peak torque requirement and the flux-weakening capability, and the upper and lower limits are derived. The slot–pole number combinations, machine inductance, axial length, and number of turns are optimized to reduce the total copper and iron losses over the NEDC. It has been also shown that a higher inductance close to the upper limits and low flux density in the stator core has a crucial effect in reducing the total energy loss over the NEDC. It should be emphasized that conventional design methodologies that aim to maximize efficiency in the region close to the rated operating condition may lead to higher energy losses over the NEDC. The experimental results with the prototype machine have validated the proposed design method.

REFERENCES

[1] C. C. Chan, "An overview of electric vehicle technology," *Proc. IEEE*, vol. 81, no. 9, pp. 1202–1213, Sep. 1993.

[2] J. G. W. West, "DC, induction, reluctance and PM motors for electric vehicles," *Power Eng. J.*, vol. 8, no. 2, pp. 77–88, 1994.

[3] S. M. Lukic and A. Emadi, "Modeling of electric machines for automotive applications using efficiency maps," in *Proc. Elect. Insul. Conf. Elect. Manuf. Coil Winding Technol. Conf.*, 2003, pp. 543–550.

[4] J. Fenton and R. Hodkinson, "Lightweight electric/hybrid vehicle design: Automotive engineering series," in *Current EV Design Approaches*. Oxford, U.K.: Butterworth-Heinemann, 2000.

[5] H. Neudorfer, N. Wicker, and A. Binder, "Comparison of three different electric powertrains for the use in hybrid electric vehicles," in *Proc. IET Conf. Power Electron., Mach. Drives*, 2008, pp. 510–514.

[6] Z. Q. Zhu and D. Howe, "Electrical machines and drives for electric, hybrid, and fuel cell vehicles," *Proc. IEEE*, vol. 95, no. 4, pp. 746–765, Apr. 2007.

[7] K. T. Chau, C. C. Chan, and C. Liu, "Overview of permanent-magnet brushless drives for electric and hybrid electric vehicles," *IEEE Trans. Ind. Electron.*, vol. 55, no. 6, pp. 2246–2257, Jun. 2008.

[8] Z. Q. Zhu and C. C. Chan, "Electrical machine topologies and technologies for electric, hybrid, and fuel cell vehicles," in *Proc. IEEE VPPC*, Sep. 2008, pp. 1–6.

[9] F. Biais and P. Langry, "Optimization of permanent magnet traction motor for electric vehicle," in *Proc. 15th EVS*, Brussels, Belgium, Oct. 1998, 13 p. [CD-ROM].

[10] Y. Amara, L. Vido, M. Gabsi, E. Hoang, A. H. Ben Ahmed, and M. Lecrivain, "Hybrid excitation synchronous machines: Energy-efficient solution for vehicles propulsion," *IEEE Trans. Veh. Technol.*, vol. 58, no. 5, pp. 2137–2149, Jun. 2009.

[11] J. de Santiago, H. Bernhoff, B. Ekergård, S. Eriksson, S. Ferhatovic, R. Waters, and M. Leijon, "Electrical motor drivelines in commercial all-electric vehicles: A review," *IEEE Trans. Veh. Technol.*, vol. 61, no. 2, pp. 475–484, Feb. 2012.

[12] S. Kreuawan, F. Gillon, and P. Brochet, "Comparative study of design approach for electric machine in traction application," *Int. Rev. Elect. Eng.*, vol. 3, no. 3, pp. 455–465, Jun. 2008.

[13] E. Sulaiman, T. Kosaka, and N. Matsui, "Design and performance of 6-slot 5-pole PMFSM with hybrid excitation for hybrid electric vehicle applications," in *Proc. Int. Power Electron. Conf.*, 2010, pp. 1962–1968.

[14] P. Morrison, A. Binder, and B. Funieru, "Drive train design for medium-sized zero emission electric vehicles," in *Proc. EPE Conf.*, Sep. 2009, pp. 1–10.

[15] X. Yuan and J. Wang, "Torque distribution strategy for a front and rear wheel driven electric vehicle," *IEEE Trans. Veh. Technol.*, vol. 61, no. 8, pp. 3365–3374, Oct. 2012.

[16] J. Wang, X. P. Xia, and D. Howe, "Three-phase modular permanent magnet brushless machine for torque boosting on a down-sized ICE vehicle," *IEEE Trans. Veh. Technol.*, vol. 54, no. 3, pp. 809–816, May 2005.

[17] A. M. El-Refaie and T. M. Jahns, "Optimal flux-weakening in surface PM machines using concentrated windings," *IEEE Trans. Ind. Appl.*, vol. 41, no. 3, pp. 790–800, May/Jun. 2005.

[18] A. Vagati, G. Pellegrino, and P. Guglielmi, "Comparison between SPM and IPM motor drives for EV applications," in *Proc. Int. Conf. Elect. Mach.*, Sep. 2010, pp. 1–6.

[19] J. Cros and P. Viarouge, "Synthesis of high performance PM machines with concentrated windings," *IEEE Trans. Energy Convers.*, vol. 17, no. 2, pp. 248–253, Jun. 2002.

[20] J. K. Tangudu, T. M. Jahns, and A. El-Refaie, "Unsaturated and saturated saliency trends in fractional-slot concentrated-winding interior permanent magnet machines," in *Proc. IEEE ECCE*, 2010, pp. 1082–1089.

[21] J. K. Tangudu, T. M. Jahns, and T. P. Bohn, "Design, analysis and loss minimization of a fractional-slot concentrated winding IPM machine for traction applications," in *Proc. IEEE ECCE*, 2011, pp. 2236–2243.

[22] W. L. Soong and N. Ertugrul, "Field weakening performance of interior permanent magnet motors," *IEEE Trans. Ind. Appl.*, vol. 38, no. 5, pp. 1251–1258, Sep./Oct. 2002.

[23] J. Wang, K. Atallah, Z. Q. Zhu, and D. Howe, "Modular 3-phase permanent magnet brushless machines for in-wheel applications," *IEEE Trans. Veh. Technol.*, vol. 57, no. 5, pp. 2714–2720, Sep. 2008.

[24] K. Atallah, J. Wang, and D. Howe, "Torque ripple minimisation in modular permanent magnet brushless machines," *IEEE Trans. Ind. Appl.*, vol. 39, no. 6, pp. 1689–1695, Jul. 2003.

[25] T. Oikawa, T. Tajima, K. Matsumoto, H. Akita, H. Kawaguchi, and H. Kometani, "Development of high efficiency brushless DC motor with new manufacturing method of stator for compressors," in *Proc. 16th Int. Compressor Eng. Conf.*, 2002, p. CD12-4.

[26] A. G. Jack, B. C. Mecrow, P. G. Dickinson, and D. Stephenson, "Permanent-magnet machines with powdered iron cores and prepressed windings," *IEEE Trans. Ind. Appl.*, vol. 36, no. 4, pp. 1077–1084, Jul./Aug. 2000.

[27] P. H. Mellor, R. Wrobel, and D. Holliday, "A computationally efficient iron loss model for brushless AC machines that caters for rated flux and field weakened operation," in *Proc. IEEE IEMDC*, May 2009, pp. 490–494.

[28] S. S. Williamson, A. Emadi, and K. Rajashekara, "Comprehensive efficiency modeling of electric traction motor drives for hybrid electric vehicle propulsion applications," *IEEE Trans. Veh. Technol.*, vol. 56, no. 4, pp. 1561–1572, Jul. 2007.

[29] G. Friedrich, "Comparative study of three control strategies for the synchronous salient poles and wound rotor machine in automotive applications with on board energy," in *Proc. 5th Int. Conf. Power Electron. Variable-Speed Drives*, 1994, pp. 706–709.

[30] J. Wang, K. Atallah, R. Chin, W. M. Arshad, and H. Lendenmann, "Rotor eddy current loss in permanent magnet brushless AC machines," *IEEE Trans. Magn.*, vol. 46, no. 7, pp. 2701–2707, Nov./Dec. 2010.

[31] J. D. Ede, K. Atallah, G. W. Jewell, J. Wang, and D. Howe, "Effect of axial segmentation of the permanent magnets on the rotor loss of modular brushless machines," *IEEE Trans. Ind. Appl.*, vol. 43, no. 5, pp. 1207–1213, Sep./Oct. 2007.

Jiabin Wang (SM'03) received the B.Eng. and M.Eng. degrees from Jiangsu University of Science and Technology, Zhengjiang, China, in 1982 and 1986, respectively, and the Ph.D. degree from the University of East London, London, U.K., in 1996, all in electrical and electronic engineering.

He is currently a Professor of electrical engineering with The University of Sheffield, Sheffield, U.K. From 1986 to 1991, he was with the Department of Electrical Engineering, Jiangsu University of Science and Technology, where he was appointed a Lecturer in 1987 and an Associated Professor in 1990. He was a Postdoctoral Research Associate with The University of Sheffield from 1996 to 1997 and a Senior Lecturer with the University of East London from 1998 to 2001. His research interests range from motion control to electromagnetic devices and their associated drives in applications ranging from automotive, household appliances, to aerospace sectors.

Xibo Yuan (S'09–M'11) received the B.S. degree in electrical engineering from China University of Mining and Technology, Xuzhou, China, in 2005 and the Ph.D. degree in electrical engineering from Tsinghua University, Beijing, China, in 2010.

From 2007 to 2008, he was a Visiting Scholar with the Center for Power Electronics Systems, Virginia Polytechnic Institute and State University, Blacksburg. During 2010 and 2011, he was a Postdoctoral Research Associate with the Electrical Machines and Drives Research Group, Department of Electronic and Electrical Engineering, The University of Sheffield, Sheffield, U.K. Since 2011, he has been a Lecturer with the Electrical Energy Management Group, Department of Electrical and Electronic Engineering, University of Bristol, Bristol, U.K. His research interests include power electronics, wind power generation, control of high-power multilevel converters, sensorless drives of induction motors and permanent-magnet motors, control of electric vehicles, and other electric aircraft technologies.

Kais Atallah received the Ingénieur d'Etat degree in electrical power engineering from the École Nationale Polytechnique, Algiers, Algeria, and the Ph.D. degree from The University of Sheffield, Sheffield, U.K.

From 1993 to 2000, he was a Research Associate with the Department of Electronic and Electrical Engineering, The University of Sheffield, where he is currently a Reader. His research interests include fault-tolerant permanent-magnet drives for aerospace, magnetic gearing, and "pseudo" direct-drive electrical machines.